



Application of partially coherent wavefront propagation calculations for design of coherence-preserving synchrotron radiation beamlines

Oleg Chubar*, Yong S. Chu, Konstantine Kaznatcheev, Hanfei Yan

NSLS-II, Brookhaven National Laboratory, Upton, NY 11973, USA

ARTICLE INFO

Available online 8 December 2010

Keywords:

Synchrotron radiation
Coherence
Wave optics
Microscopy

ABSTRACT

Ultra-low emittance third-generation synchrotron radiation (SR) sources, such as NSLS-II and MAX-IV, will offer excellent opportunities for further development of experimental techniques exploiting X-ray coherence. However, even in these new SR sources, the radiation produced by relativistic electrons (in undulators, wigglers and bending magnets) will remain only partially coherent in the X-ray spectral range. “Extraction” of “coherent portion” of the radiation flux and its transport to sample without loss of coherence must be performed by dedicated SR beamlines, optimized for particular types of experiments. Detailed quantitative prediction of partially coherent X-ray beam properties at propagation through optical elements, which is required for the optimization of such beamlines, can only be obtained from accurate and efficient physical-optics based numerical simulations. Examples of such simulations, made for NSLS-II beamlines, using “Synchrotron Radiation Workshop” (SRW) computer code, are presented. Special attention is paid to the numerical analysis of the basic properties of partially coherent undulator radiation beam and its distinctions from the Gaussian beam. Performance characteristics of importance for particular beamlines, such as radiation spot size and flux at sample vs size of secondary source aperture for high-resolution microscopy beamlines, are predicted by the simulations.

© 2010 Elsevier B.V. All rights reserved.

1. Introduction

Over the past decade, many novel experimental techniques relying on X-ray coherence either for scattering or for imaging (e.g. X-ray photon correlation spectroscopy, scanning X-ray microscopy, phase-contrast and coherent diffraction imaging) have emerged. Evidently, traditional beamline ray-tracing analysis has to be extended beyond geometrical optics—to include accurate calculation of wave-optical characteristics of SR sources, and to allow for simulation of fully and partially coherent SR wavefront propagation through optical elements of a beamline.

After the first wave-optics computer codes for simulation of transversely coherent SR wavefront propagation became available [1–3], they have quickly found a number of important practical applications, such as optimization of infrared beamlines in 3rd generation SR sources [4–6], simulation and analysis of free-electron laser wavefronts [7,8], and electron beam diagnostics [3,9,10]. In most of these applications, however, fully transversely coherent wavefronts were treated.

In this paper, we numerically calculate and analyze the basic characteristics of partially coherent X-ray range Undulator Radiation (UR), i.e. the apparent angular divergences and “source sizes”

of the UR beam in a low-emittance synchrotron source, paying special attention to deviations from the predictions of the Gaussian Schell model [11]. After this, we extend and complement the partially coherent UR wavefront propagation analysis that was performed recently [12] for the conceptual design parameters of the Hard X-ray Nanoprobe (HXN) beamline at NSLS-II.

Our calculations are based on the general method of summing up intensities after numerical propagation of frequency-domain UR electric fields emitted by individual (macro-) electrons, distributed in the 6D phase space of the electron beam. We note that, as different from the analytical approach [13], our calculations include the effect of electron beam energy spread and are not limited by the consideration of only resonant photon energy values of UR harmonics. The calculations were performed using SRW code [2,3].

2. Calculation examples

2.1. Apparent angular divergences and “source sizes” of partially coherent undulator radiation beam

For a large number of beamline design tasks, accurate values of horizontal and vertical angular divergences and “source sizes” of UR beam are necessary. These values have to include contributions of angular divergences and diffraction-limited source sizes of single-electron UR, as well as the divergences and sizes of finite-emittance

* Corresponding author. Tel.: +1 631 344 4525.
E-mail address: chubar@bnl.gov (O. Chubar).

electron beam. Even though approximate values of the divergences and source sizes can be obtained from analytical formulas [14,15], more accurate values may require numerical partially coherent wavefront propagation calculations. An example of such calculations, performed for two slightly different photon energy values at the 5th harmonic of radiation from a U20 (20 mm period, 3 m long) hybrid in-vacuum undulator of NSLS-II, is presented in Fig. 1. One of the photon energy values used (10.009 keV) is exactly the on-axis resonant photon energy of the single-electron UR (5th harmonic), whereas the other value (9.996 keV) was chosen to be close to the peak of the UR spectral flux collected through a $100\text{ }\mu\text{rad}$ (h) \times $50\text{ }\mu\text{rad}$ (v) angular aperture, which is comparable to a typical angular acceptance of an undulator-based hard X-ray beamline in a 3rd generation source (Fig. 1a).

To estimate the X-ray beam angular divergences at these two photon energies, we calculated the corresponding UR intensity distribution for an observation plane located relatively far (at 30 m) from the undulator (Fig. 1b and c). Then, in order to estimate the apparent X-ray beam source sizes, we considered a simple 1:1 focusing scheme consisting of one ideal lens located at 30 m from the undulator, and calculated, using the partially coherent wavefront propagation method, the intensity distributions in the image plane of this scheme, i.e. at 60 m from the undulator (Fig. 1d and e). For these calculations, the “day 1” horizontal and vertical emittances and energy spread of the electron beam (0.9 nm, 8 pm and 8.9×10^{-4} , respectively), and the nominal horizontal and vertical beta-function values of NSLS-II low-beta straight section (2.02 m and 1.06 m, respectively) were used. The FWHM values of

the horizontal and vertical angular divergences (θ_x , θ_y) and source sizes (s_x , s_y), obtained from these calculations, are given in Fig. 1f–i.

In addition to the observation that the maximal UR flux from a finite-emittance electron beam collected through a finite aperture does not correspond to the on-axis resonant photon energy of single-electron UR [16], we also note that in the vertical plane, the multi-electron UR intensity distributions both at a distance from the undulator (Fig. 1b, c and g), and in the 1:1 image plane (Fig. 1d, e and i) differ from Gaussian, especially for photon energies not equal to the on-axis resonant energy of a single-electron UR harmonic.

It can be useful to estimate apparent “phase-space volume” occupied by this partially coherent UR beam and to compare it to the well-known values for the fully coherent Gaussian beam at the same wavelength ($\lambda/4\pi$). Such comparisons, performed both for RMS ($\sigma_{ph}\sigma'_{ph}$) and FWHM ($s_{ph}s'_{ph}$) values of the corresponding intensity distributions, are presented in Table 1. In the second column of Table 1, ratios of the horizontal and vertical electron beam emittance (ϵ_e) to the phase-space volume of a fully coherent Gaussian beam at ~ 10 keV photon energy are given. We see that in the horizontal plane, the phase-space volume of the resulting photon beam is dominated by the volume occupied by the electron beam. On the other hand, in the vertical plane, the electron beam emittance is small, and the “excessive” phase-space volume of the resulting photon beam (compared to that of the coherent Gaussian beam) is explained by deviation of the single-electron UR distribution from Gaussian, and by contribution of the electron beam energy spread to the UR angular divergence and the source size.

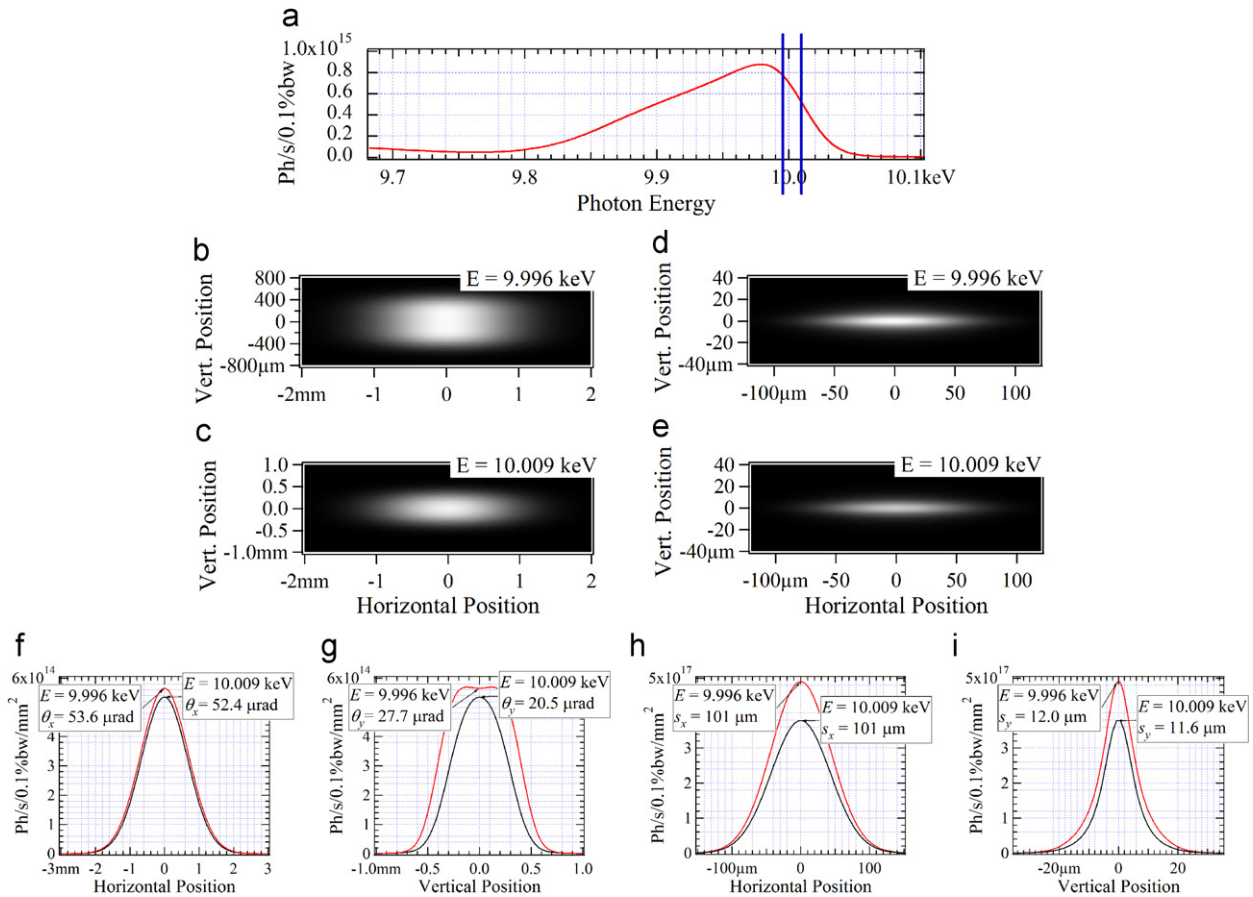


Fig. 1. Spectral intensity distributions of radiation from NSLS-II U20 in-vacuum undulator, tuned to have 5th harmonic at ~ 10 keV (for this, U20 gap has to be set to ~ 5.8 mm, which is a bit larger than the 5 mm minimum gap value): (a) spectral flux collected through $100\text{ }\mu\text{rad}$ (horizontal) \times $50\text{ }\mu\text{rad}$ (vertical) angular aperture; (b and c) intensity distributions at 30 m from undulator at 9.996 keV photon energy (shown by left vertical line in (a)) and at 10.009 keV photon energy (shown by right line in (a)); (d and e) intensity distributions in 1:1 image plane; (f and h) horizontal cuts of intensity distributions at 30 m from undulator (f) and in 1:1 image plane (h); and (g and i) vertical cuts of intensity distributions at 30 m from undulator (g) and in 1:1 image plane (i).

Table 1
Comparison of apparent phase-space volume occupied by partially coherent UR beam at ~ 10 keV photon energy (at 5th undulator harmonic) to that of fully coherent Gaussian beam, for case of 0.9 nm (8 μ m) horizontal (vertical) emittance and 8.9×10^{-4} relative energy spread of 3 GeV electron beam.

Phase-space volume ratios	$\varepsilon_e \cdot 4\pi/\lambda$	$\sigma_{ph}\sigma'_{ph} \cdot 4\pi/\lambda$		$[S_{ph}S'_{ph}/(2.35)^2]4\pi/\lambda$	
		$\lambda = \lambda_n$	$\lambda \approx 1.0013 \lambda_n^a$	$\lambda = \lambda_n$	$\lambda \approx 1.0013 \lambda_n^a$
Horizontal plane	91.2	97.3	99.5	97.2	99.3
Vertical plane	0.81	$\sim 5.1^b$	$\sim 6.5^b$	4.4	6.1

^a In terms of harmonic number ($n=5$), number of undulator periods ($N=150$) and on-axis resonant wavelength of the harmonic ($\lambda_n \approx 1.2387$ Å), this wavelength value is $\lambda \approx (1+0.97/(nN))\lambda_n$.

^b Because of slow convergence, the RMS values for the vertical plane were calculated for the portions of intensity distributions containing $\sim 99\%$ of total flux.

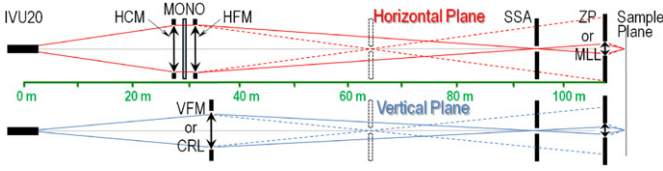


Fig. 2. Conceptual optical scheme of Hard X-ray Nanoprobe beamline at NSLS-II.

From the phase-space volumes presented in Table 1 and the spectral flux shown in Fig. 1a, one can estimate the apparent brightness and the “transversely coherent flux portion” [15] of the partially coherent UR source. For the resonant photon energy (10.009 keV), the estimated apparent brightness is $\sim 2.9 \times 10^{20}$ ph/s/1%bw/mrad²/mm² and the coherent flux $\sim 1.1 \times 10^{12}$ ph/s/1%bw (which represents $\sim 2 \times 10^{-3}$ fraction of the total flux emitted at that photon energy); for the “red-shifted” photon energy (9.996 keV) the apparent brightness and the coherent flux values are, respectively, $\sim 3.3 \times 10^{20}$ ph/s/1%bw/mrad²/mm² and $\sim 1.3 \times 10^{12}$ ph/s/1%bw (the latter value representing $\sim 1.6 \times 10^{-3}$ fraction of the corresponding total flux).

2.2. Performance estimation of ultra-high resolution hard X-ray microscopy beamline

The conceptual optical scheme of the NSLS-II HXN beamline is presented in Fig. 2. The beamline will use radiation from a 20 mm period 3 m long in-vacuum undulator installed in a low-beta straight section of NSLS-II. The first optical element is a Horizontal Collimating Mirror (HCM) located at ~ 27.2 m from the (center of) undulator. The HCM provides a nearly parallel X-ray beam on a horizontally deflecting Si(1 1 1) double-crystal pseudo-channel-cut Monochromator (MONO). Since the horizontal angular divergence of the collimated X-ray beam (~ 3.7 μ rad) is much smaller than the Darwin-width of the Si(1 1 1) reflection for Pi-polarization (~ 24.5 μ rad at 10 keV photon energy), the monochromator does not clip the transverse phase space of the beam. After the monochromator, the beam is focused by Horizontally and then by Vertically Focusing Mirrors (HFM and VFM) located at ~ 31.3 and ~ 32.8 m from the undulator. The secondary source, i.e. anastigmatic waist in the horizontal and vertical planes, “improved” by a rectangular Secondary Source Aperture (SSA), can be located either at ~ 62 – 65 m (when the HFM and VFM focal lengths are ~ 31 – 34 and ~ 15 – 16 m, respectively), or at ~ 92 – 94 m from the undulator (when the HFM and VFM focal lengths are ~ 61 – 63 and ~ 21 m). A 1D parabolic Be Compound Refractive Lens (CRL) [17,18] may be used in place of the VFM. The final nanofocusing optics – Zone Plate (ZP) or Multilayer Laue Lens (MLL) – are located at ~ 105 – 109 m from the undulator.

The results of partially coherent wavefront propagation calculations performed for two different beamline cases are presented in Fig. 3. In the first case, the SSA is located at 62 m from the undulator,

and its horizontal size is 50 μ m (in the vertical direction the SSA is fully open), and a hypothetical nanofocusing optics with ~ 18.14 mm focal length and 150 μ m aperture diameter is located at 105 m (the wavefront propagation simulation results for that case are shown in Fig. 3a–d). In the second case, the SSA is at 94 m; its horizontal and vertical sizes are 12 μ m and 16 μ m, respectively, with the nanofocusing optics located at 109 m (simulation results for that case are presented in Fig. 3a, e–g). At these calculations, all beamline optics, including the nanofocusing optics, were simulated by ideal perfectly transmitting lenses; the monochromator was assumed to be perfect too. On the other hand, geometrical apertures of all optical elements were carefully respected. Such approximations were used purposely, in order to “observe” pure effects related to partial coherence of the source, to trace losses on apertures, and to estimate “ultimate performance” of the beamline. The undulator was assumed to provide a spectral peak of the 5th harmonic at ~ 10 keV photon energy, as this was the case in the calculations discussed in the previous section.

Fig. 3a shows the UR intensity distribution at the HCM, with the mirror geometrical aperture indicated by a rectangle in the image plot (on the left) and by vertical lines in the intensity cuts graph (on the right). Fig. 3b and e presents the intensity distributions just before the SSA (which is indicated by lines and a rectangle); Fig. 3c and f gives the intensity distributions in the plane of the nanofocusing optics, with the small circles in the image plots representing the apertures of these optics and Fig. 3d and g provides the intensity distributions “at the sample”. The spectral flux, obtained using the approximations described above, is $\sim 7.4 \times 10^{14}$ ph/s/1%bw after the HCM, $\sim 2.9 \times 10^{14}$ ($\sim 1.7 \times 10^{13}$) ph/s/1%bw after the SSA, and $\sim 2.0 \times 10^{12}$ ($\sim 3.6 \times 10^{12}$) ph/s/1%bw within the nanofocusing optics aperture in the first (second) simulation case.

We note that the sizes of intensity distributions “at the sample” (Fig. 3d and g) are close to the diffraction limit—in the first simulation case, the horizontal FWHM spot size is ~ 22 nm (for a 50 μ m horizontal SSA size), and the vertical FWHM size is ~ 16 nm; in the second case, both the horizontal and vertical FWHM sizes are ~ 17 nm. The estimated FWHM diffraction-limited spot size for the considered nanofocusing optics is ~ 15 nm at a 10 keV photon energy.

Since the diffraction-limited spot size at the sample can be reached only by a coherent wavefront, it is interesting to estimate degree of transverse coherence of the wavefront within the aperture of nanofocusing optics. Such estimations can be done, e.g. by simulating wavefront propagation through Young’s 2-slit interference scheme, with the slits located at a longitudinal position of the nanofocusing optics. Fig. 4a shows the visibility of fringes in a scheme with two vertical (horizontally separated) slits vs the horizontal size of the SSA located at 94 m, in comparison with predictions of the van Cittert–Zernike theorem, assuming that a fully incoherent extended constant-brightness source is located at the SSA. We can notice only a small difference between the partially coherent UR wavefront propagation simulation results and the van Cittert–Zernike theorem predictions, because the

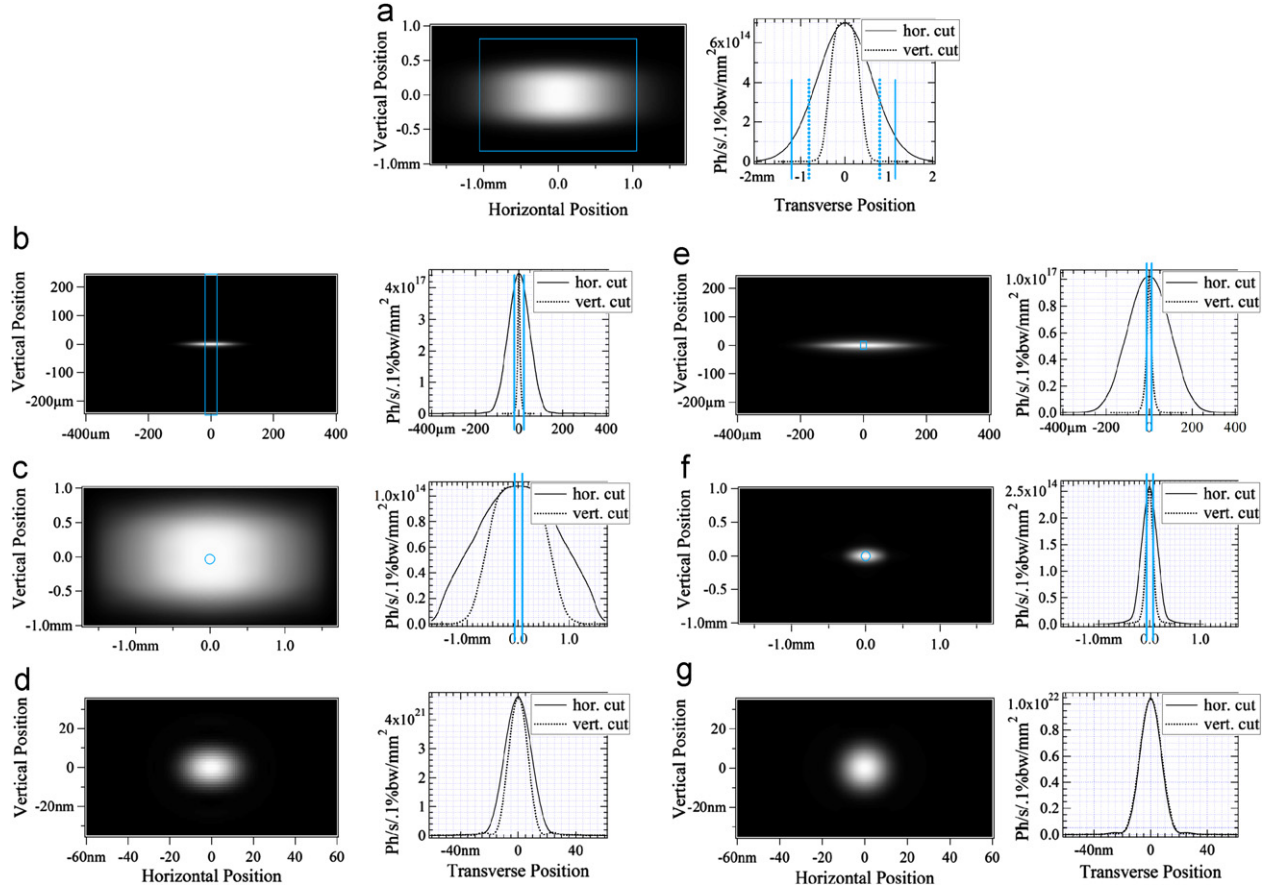


Fig. 3. Intensity distribution image plots (on the left) and horizontal and vertical intensity cuts (on the right), at different beamline locations: (a) at HCM; (b) before SSA located at 62 m from undulator; (c) before nanofocusing optics in case of 50 μm horizontal size of SSA located at 62 m; (d) at sample for SSA location and size as in (b) and (c); (e) before SSA located at 94 m; (f) before nanofocusing optics in the case of 12 μm horizontal and 16 μm vertical size of SSA located at 94 m; and (g) at sample, for SSA location and sizes as in (e) and (f).

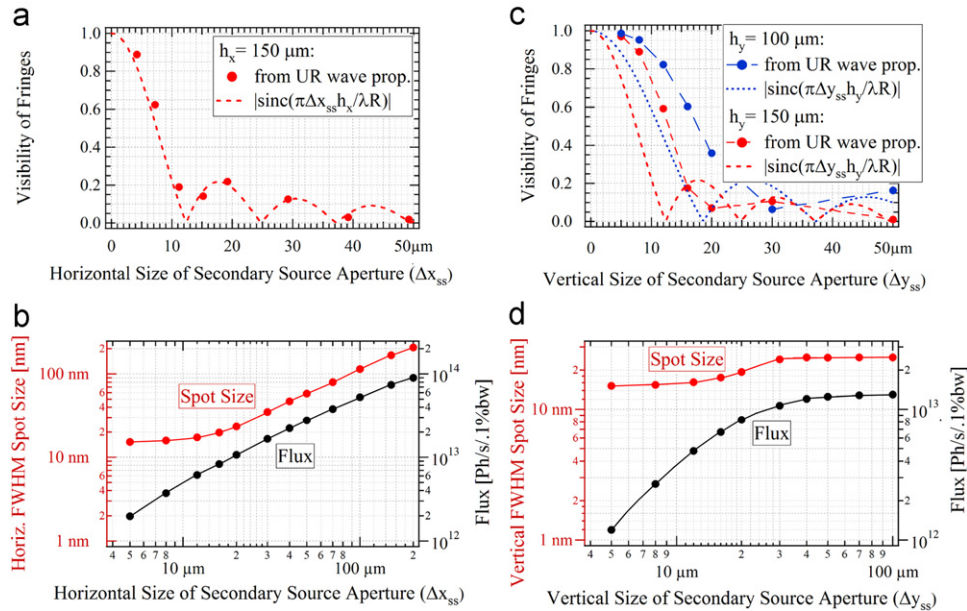


Fig. 4. (a) Visibility of fringes in interference patterns calculated for virtual Young's schemes with two vertical slits, separated by $h_x = 150 \mu\text{m}$ horizontal distance, as function of horizontal SSA size; (b) horizontal FWHM spot size and flux within 150 μm aperture of nanofocusing optics as function of horizontal SSA size at 30 μm vertical SSA size; (c) visibility of fringes in interference patterns of virtual Young's schemes with two horizontal slits separated by $h_y = 100$ and 150 μm vertical distance as function of vertical SSA size; and (d) vertical FWHM spot size and flux vs vertical SSA size at 20 μm horizontal SSA size (SSA is located at 94 m; nanofocusing optics at 109 m in all cases).

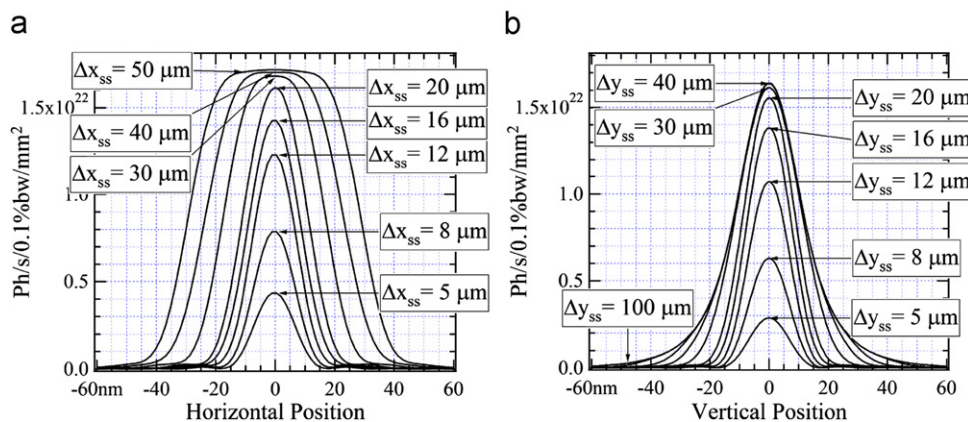


Fig. 5. Horizontal (a) and vertical (b) cuts of intensity distributions at sample for different horizontal (Δx_{ss}) and vertical (Δy_{ss}) sizes of SSA located at 94 m, assuming final focusing by ideal lenses with 18.14 mm focal length and 150 μm aperture diameter.

intensity distribution at the SSA in this case is almost constant in the horizontal direction within the horizontal SSA sizes used at these calculations (see Fig. 3e), and because the photon beam coherence in the horizontal direction is relatively poor. The horizontal FWHM spot size obtained for nanofocusing optics simulated by an ideal lens with an 18.14 mm focal length and 150 μm aperture diameter, and the flux within the aperture of the nanofocusing optics are shown in Fig. 4b, also as functions of the horizontal SSA size (at a 30 μm vertical SSA size). The visibility of fringes in the vertical plane, vertical spot size and flux within the nanofocusing optics aperture vs vertical SSA size (at a 20 μm horizontal SSA size) are presented in Fig. 4c and d. We see a significant deviation from the van Cittert–Zernike theorem in this case, which is explained by the small size and relatively high degree of coherence of the photon beam in the vertical direction at the SSA.

Finally, in Fig. 5 we present horizontal (vertical) cuts of intensity distributions “at the sample” at different horizontal (vertical) SSA sizes. One can trace variations of the intensity distribution shapes in different regimes, from the diffraction limit to the “high throughput”. In the high throughput regime (e.g. at the SSA sizes larger than $\sim 30 \mu\text{m}$), the horizontal and vertical intensity cuts differ in shape. We note that the use of the vertical SSA with ~ 20 – $30 \mu\text{m}$ size reduces the useful flux in the spot at the sample quite insignificantly (see Fig. 4d); however, it substantially removes “tails” of the intensity distribution in the vertical direction.

3. Conclusions

We demonstrated feasibility and utility of the partially coherent wavefront propagation simulations from an undulator to a sample for the design and performance prediction of coherence preserving X-ray beamlines. The focus in this paper was made on peculiarities of partially coherent undulator radiation in 3rd generation SR sources. The analysis was performed for “ideal” optical elements, even though optical element imperfections can be easily incorporated

into the calculation method used. Current implementation of the partially coherent wavefront propagation method may still require significant CPU time for the simulations; however we believe that very large potentials exist for improving the computational efficiency and for further extending the range of applications of this method.

Acknowledgements

The authors would like to thank Ruben Reininger, Andrei Fluerașu, David Shapiro, Secilia Sanchez-Hanke, Larry Margulies, Lonny Berman, Steve Hulbert and Qun Shen (NSLS-II/NSLS) for support and fruitful discussions. This work was also supported by US DOE, Contract no. DE-AC02-98CH10886.

References

- [1] J. Bahrtdt, Appl. Opt. 36 (19) (1997) 4367.
- [2] O. Chubar, P. Elleaume, Proceedings of EPAC-98, p. 1177.
- [3] O. Chubar, P. Elleaume, S. Kuznetsov, A. Snigirev, Proc. SPIE Int. Soc. Opt. Eng. 4769 (2002) 145.
- [4] P. Dumas, et al., Infrared Phys. Technol. 49 (2006) 152.
- [5] P. Roy, et al., Infrared Phys. Technol. 49 (2006) 139.
- [6] O. Chubar, et al., SRI-2006, AIP Conference Proceedings 879, p. 607.
- [7] J. Bahrtdt, Phys. Rev. ST Accel. Beams 10 (2007) 060701.
- [8] O. Chubar, et al., Nucl. Instr. and Meth. A 593 (2008) 30.
- [9] O. Chubar, et al., Proceedings of DIPAC-2001, p. 88.
- [10] M.-A. Tordeux, et al., Proceedings of DIPAC-2007, p. 180.
- [11] R. Coisson, Appl. Opt. 34 (5) (1995) 904.
- [12] O. Chubar, Y.S. Chu, K. Kaznatcheev, H. Yan, SRI-2009, AIP Conference Proceedings 1234, p. 75.
- [13] G. Geloni, et al., Nucl. Instr. and Meth. A 588 (3) (2008) 463.
- [14] K.-J. Kim, AIP Conf. Proc. 184 (1989) 565.
- [15] K.-J. Kim, Characteristics of synchrotron radiation, X-Ray Data Booklet, LBNL, 2nd ed., University of California, Berkeley, 2001.
- [16] P. Elleaume, Undulator radiation, in: H. Onuki, P. Elleaume (Eds.), Undulators, Wigglers and their Applications, Taylor and Francis, 2003, pp. 69–107.
- [17] A. Snigirev, V. Kohn, I. Snigireva, B. Lengeler, Nature 384 (1996) 49.
- [18] B. Lengeler, et al., J. Synchrotron Radiat. 6 (1999) 1153.